

Additive Manufacturing of Al-12Si Alloy Via Pulsed Selective Laser Melting

R. CHOU,¹ J. MILLIGAN,¹ M. PALIWAL,¹ and M. BROCHU^{1,2}

1.—Department of Mining and Materials Engineering, McGill University, Montreal, QC H3A 0C5, Canada. 2.—e-mail: mathieu.brochu@mcgill.ca

Additive manufacturing (AM) of metallic materials is experiencing a research and commercialization craze in almost all industrial sectors. However, to date, AM has been limited to a small numbers of alloys. With respect to aluminum, two alloys received some attention: Al-12Si and Al-10Si-1Mg. In both cases, fully dense components have been achieved using a continuous-wave selective laser melting system. In this article, a new approach of selective laser melting using a pulsed-laser source as opposed to a continuous-wave laser is proposed. Pulse selective laser melting (P-SLM) would allow for greater control over the heat input and thus further optimization possibilities of the microstructure. P-SLM was demonstrated using the Al-12Si system. Si refinement below 200 nm was achieved throughout the component. Density up to 95% and high hardness of above 135 HV were obtained. The solidification mechanism is also explained.

INTRODUCTION

Unlike subtractive manufacturing techniques, where end components are obtained by removing materials from the starting block, additive manufacturing (AM) produces parts through material addition processes that build up components layer by layer. These additive processes have been getting significant interest over the last few years because of their transformative advantages. Several works and reviews on the disruptive nature of the technology, the different processes, and the microstructure–processing–properties relationships of numerous alloys can be found in the literature.^{1–4}

AM of aluminum and its alloys has a bright future for aerospace and ultra-lightweight components, from the capability to fabricate components with complex internal geometries and lattice structures, or simply to reduce the buy to fly ratio for expensive alloys, such as any Li-bearing alloys. However, three significant challenges currently delay wide implementation: (I) low flowability and apparent density of powder, (II) the high thermal conductivity, and (III) the native Al₂O₃ scale that forms on the powder.^{5–8} Besides powder characteristics, laser process parameters are also significant factors that govern selective laser melted (SLM) part quality and microstructure. In previous studies, considerable

work has been made toward optimizing parameters with the aim of improving the density of SLM Al-Si based alloys.^{5–7,9,10} To date, most of the work on Al-Si alloys has been focused on the Al-12Si and Al-10Si-1Mg systems with only a few studies undertaken on commercial alloy AA 6061.⁵ All reported work involved the use of continuous-wave (CW) laser power supplies. Trends observed throughout the literature on the SLM of Al-Si alloys show that in general an increase in laser power leads to an increase in final part density. The increased power facilitates melting of the powder helping to circumvent the high thermal conductivity and reflectivity of Al. Most studies in the literature, however, focus on the mechanical properties achieved from the builds apart from the solidification aspects of the process.

Modifying and controlling the solidification kinetics could show excellent promise for the control of the Si morphology throughout the microstructure, which would have beneficial aspects for reducing crack-initiation sites and, hence, improved ductility.¹¹ One route to offer increased control over the kinetics is the use of a pulsed laser system, allowing for greater control of the heat input. The short pulse duration and high pulse frequency, in combination with the small amount of material melted during each pulse, results in the evolution of

extremely rapid cooling/solidification rates and virtually no heating of the part at the macroscale. Grain refinement of Al-Si alloys by rapid solidification was previously demonstrated. Particularly, Salehi and Dehghani¹² reported that melt spinning (cooling rate of 10^7 K/s) of A413.1 yielded to the refinement of the primary Si phase down to a range between 60 nm and 100 nm. Xu et al.¹³ reported that for Al-20 wt.% Si, a refinement of the primary silicon phase to 500 nm when a cooling rate of 10^5 K/s was used. Combining these results suggests that a pulsed SLM (P-SLM) approach could yield an even finer and more homogeneous microstructure than what is obtainable by CW laser system (CW-SLM).

This study will present a process optimization and a demonstration of the modification of microstructure (Si grain refinement and shape modification) of Al-12Si using P-SLM. Literature data on the continuous-laser process will be used as benchmark for comparison with the pulse approach, in which microstructures significantly deviating from the equilibrium were obtained.

EXPERIMENTAL PROCEDURES

Two Al-12Si powders (namely S-20 and S-10) and sourced from Valimet Inc. (Stockton, CA), were used in this study. The powders were characterized with respect to (I) morphology using secondary electron imaging acquired with a Hitachi SU3500 scanning electron microscope (SEM), (II) particle size distribution using a LA-920 Horiba laser particle size analyzer, and (III) flow and apparent density using the Hall flowmeter following ASTM standards (B213-3 and B212-99) and the angle of repose methodologies. The results are summarized in Table I. Micrographs showing their representative morphologies are presented in Fig. 1a and b for powders S20 and S10, respectively.

SLM was performed using an in-house built P-SLM facility. A pulsed Nd:YAG laser ($\lambda = 1.06 \mu\text{m}$) was used to build samples using the following parameters: 0.5–4.5 kW peak laser power, 90–180 mm/min travel speed, and 150 μm spot size in an argon atmosphere. Cylindrical specimens of 5 mm diameter and 5 mm height were fabricated using a hatching distance of 0.1 mm and a layer thickness of 0.1 mm. For the build strategy, a simple bidirectional zigzag scanning pattern was

implemented, where the direction of scanning was rotated 45° between consecutive layers. The sample density was measured using the Archimedes principle and optical micrographs taken from the vertical cross section. Standard metallographic procedures were used to reveal the microstructure. A Nikon light optical microscope with Clemex Vision System, SKYSCAN 1172 Micro-CT, and a Hitachi SU3500 SEM were used to characterize the microstructures. Keller's reagent was used on the polished specimens to reveal microstructural details. The hardness of the built component was measured by means of a Clark Microhardness (CM-100AT) indenter using 100 gf and a 10-s indentation period.

RESULTS AND DISCUSSION

P-SLM Build Quality

Figure 2a and b depicts the relation between peak pulse power and component density for the S-20 and S-10 powders, respectively. For the S20 powder (Fig. 2a), as the peak laser power increases, the final density of the P-SLM parts increases from $62.8\% \pm 1.0\%$ of the theoretical density (TD) (2.65 g/cc) to a maximum of $93.8\% \pm 1.9\%$ at 4 kW. As the laser peak power increases further, the resulting density starts to decrease to a lower density of 90.7% obtained at 4.5 kW. For the S10 powder, the density versus laser peak power curve is presented Fig. 2b, which showed a similar upward/downward trend to the S-20 powder, with the highest density of $95.6\% \pm 1.0\%$ obtained at 3 kW peak laser power. In the lower peak laser power regime, due to incomplete fusion and shallow laser penetration depth, defects with irregular shapes around 200 μm wide remained in the sample, explaining the low density. In the higher laser power regime, however, the laser power was sufficient for complete melting and fusion of molten pools of each subsequent pulse. Too high of a laser power resulted in a large amount of liquid being formed, which balls due to surface tension resulting in poor build quality and lower density.^{5,9}

As demonstrated, the S10 powder required a lower peak power (3 kW) than for S-20 (4 kW) to obtain peak density. Niu and Chang¹⁴ have observed a similar phenomenon with steel power using the selective laser sintering process, in which they reported that a fully dense sintered surface could be achieved with smaller steel particles using

Table I. Summary of Al-12Si powder characteristics

Powders	Composition (wt.%)			Particle size (μm)			Flowability (s/50 g)	Angle of repose ($^\circ$)	Apparent density (%)
	Al	Si	Fe	d10	d50	d90			
S20	Bal	12	0.8	44.9	67.5	102.3	36.76	30	53.6
S10	Bal	12	0.8	11.6	21.4	58.9	No flow	50	41.5

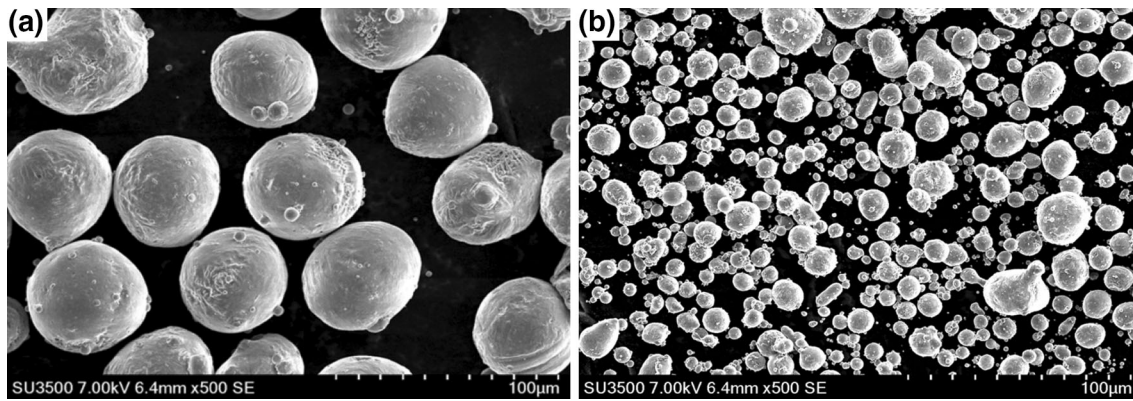


Fig. 1. SEM images of the different Al-12Si particle sizes (a) S20 and (b) S10.

lower laser power. Previous studies demonstrated that this phenomenon is due to the finer powder having a greater surface area per volume exposed to the incident laser, enhancing the laser–powder interaction leading to an increased melting reaction^{14,15} and hold true for the current work. Several authors^{16,17} have reported that the energy density required for complete melting is one of the main parameters affecting the overall density of an AM part. According to previous studies, the volumetric energy density (E) can be calculated by the following equation for the SLM process:^{16,17}

$$E = \frac{P}{vht}$$

where P is the laser power (average power in the case of the pulsed process), v is the scanning speed, h is the hatch spacing, and t is the layer thickness. The calculated energy density achieved for the optimal density for the S10 powder was 1220 J/mm³ and 1620 J/mm³ for the S20 powder. This energy density is two orders of magnitude higher than the energy densities reported in the literature for CW-SLM that achieved full density. These energy densities are on the order of 40–80 J/mm³ for the Al-12Si system. Typical travel speeds and laser powers ranged from 800 mm/s to 1400 mm/s and from 100 W to 300 W, respectively.^{5,6,10,18–20} The large energy densities, created by the pulsing process, melted a sufficient volume of material to overcome the lower apparent density of the smaller powder particles. This deeper penetration also allowed for a larger layer thickness to be employed with the powder that showed poor flowability. Typical SLM processes spread layers approximately 50 µm thick, whereas for the P-SLM process, a layer thickness of 100 µm was used. Residual porosity and defects have been attributed to the formation of oxides and their displacement into intersolid regions.⁵

Computed tomography (CT) analysis was applied to the highest density parts, to reveal the location of the remaining internal porosity. Figure 3a and b presents the side-view and top-view CT scans of the

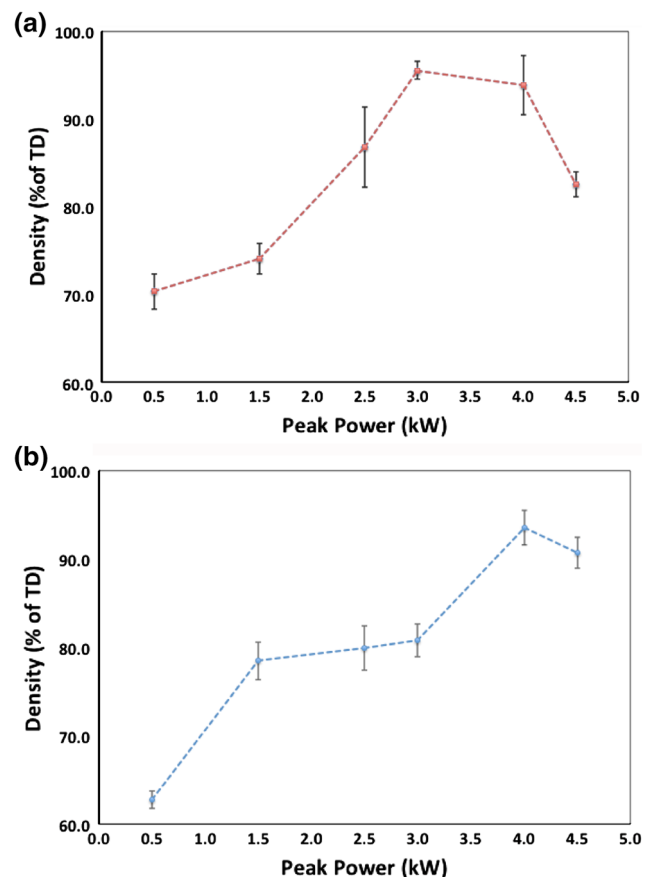


Fig. 2. The density versus peak laser power input for the two different particles sizes (a) Al-12Si S10 and (b) Al-12Si S20.

P-SLM specimen made from the S-10 powder. A broad spread of porosity throughout the three-dimensional cylindrical structure can be observed. The cross-sectional view shows pores throughout the height of the sample, whereas the top view shows that most pores are located around the edge of the sample. In many applications, for components fabricated by SLM in varying materials, the surface is treated to remove any residual roughness or

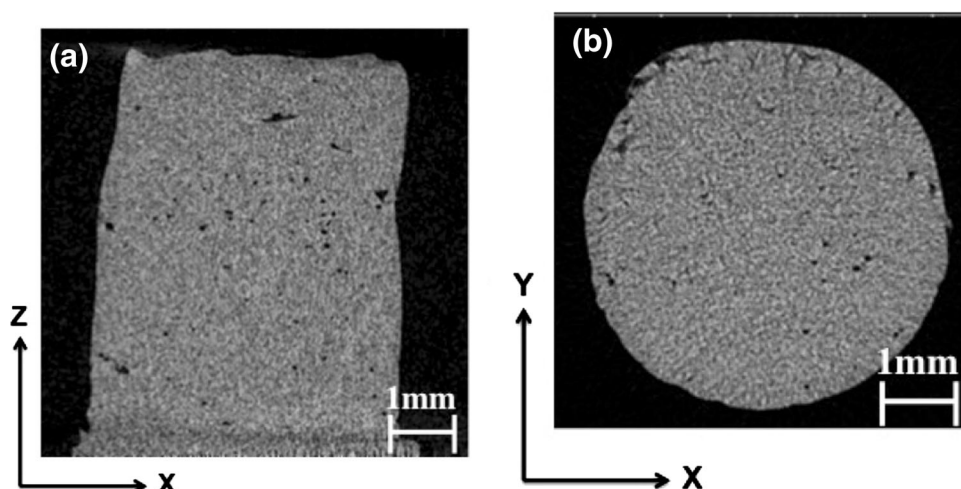


Fig. 3. CT scan images of (a) the side view and (b) top view of SLM-S10 specimen.

porosity, or to achieve application-dependent surface properties.^{18,19} Thus, if such concept were to be applied to the P-SLM components, the bulk of the surface porosity would be removed, increasing the part density further.

Solidification Microstructure

Figure 4 shows the SEM micrograph of the top view (parallel to the incident beam direction) of the microstructure of the P-SLM S-10 sample. The resultant features created by the pulsed laser beam are very different from the elongated teardrop shape molten pool microstructures caused by continuous-wave laser beam movement reported in other studies.^{10,20} In fact, the depicted microstructure consists of circular molten pools overlapping each other toward the direction of laser movement. The pulse laser induces on/off periods. The tens of millisecond gaps between each pulse allow each individual molten pool to solidify before the next laser pulse is fired.

Figure 5 shows SEM cross-section micrographs perpendicular to the build direction. It particularly focuses on an area between two incident pulses, where the upper and lower portions of the micrograph correspond to two separate pulses, denoted as pulse 1 and 2. Precisely, three distinct regions can be observed. Pulse 1 shows a fine predominantly dendritic structure with an arm spacing of 210 ± 60 nm. Pulse 2 shows a dendritic microstructure oriented with an approximate 45° from the pulse 1 layer. The measured spacing was 260 ± 60 nm, i.e., statistically similar to the pulse 1 layer. Between these two pulse layers exists a boundary of a microstructurally coarsened zone approximately $2 \mu\text{m}$ wide where the microstructure was coarsened to 600 ± 180 nm. Based on the orientation of the microstructure in the coarsened area, which appears similar to the layer above it,

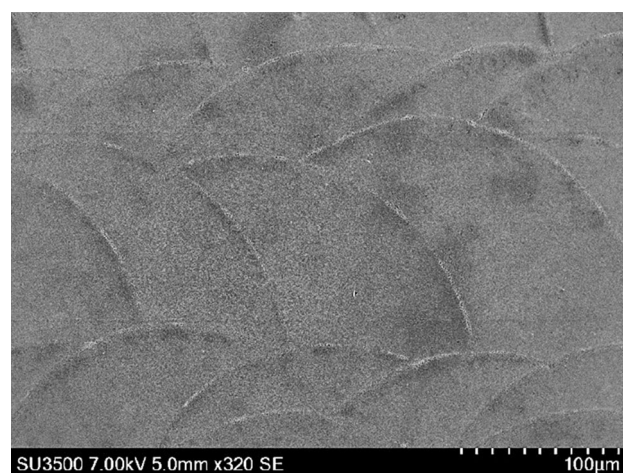


Fig. 4. The top view microstructure of the top layer after P-SLM showing subsequent pulse overlaps.

this suggests that the coarsened area is caused by a change in solidification kinetics as opposed to a solid-state growth phenomenon of the layer below it, as suggested in other work.²¹

The microstructure of a typical Al-12Si casting develops as the eutectic phase, which consists of an Al matrix with flake-like Si particles throughout. Micrographs of this structure can be readily found throughout the literature.²² During the normal casting process, the solidification rate is generally slow and the undercooling experienced is small compared with the large undercooling experienced in SLM.²³ Kang et al. studied the effect of increasing undercooling on the morphology development during the solidification of Al-13Si and hypereutectic Al-Si alloys (18 wt.%, 20 wt.%, and 25 wt.% Si).²⁴ With increasing amounts of undercooling, the growth velocities of each phase changed. At relatively low undercooling ($\Delta T < 19$ K), the growth of the eutectic phase was preferred and as undercooling

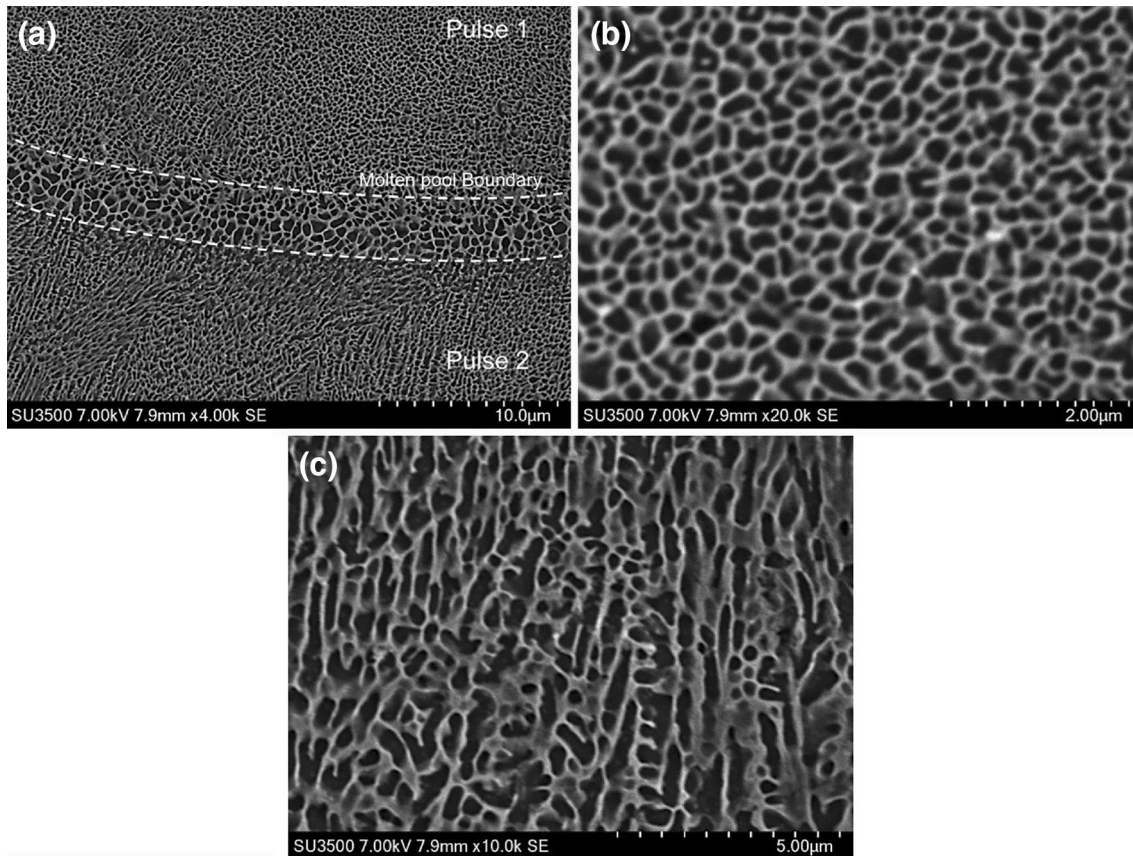


Fig. 5. Cross-section of the as built P-SLM S10 microstructure (a) showing two incident pulses and the coarsened region between the two and higher magnifications of the (b) upper and (c) lower regions.

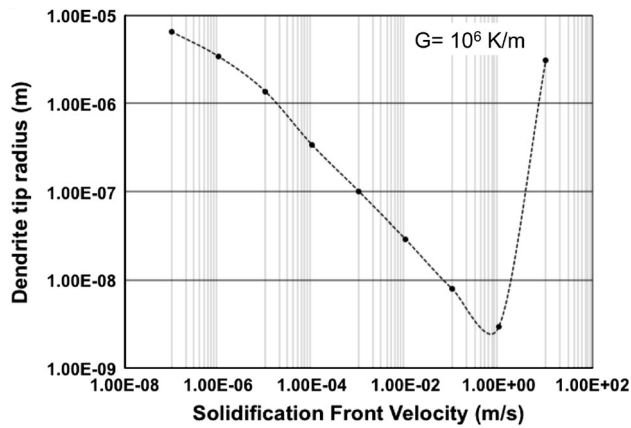


Fig. 6. The KGT model for the binary Al-Si system depicting the scale of microstructural development during solidification.

increased ($\Delta T > 19$ K), a phase change was observed from the eutectic microstructure to primary α -dendrites as the primary solidification phase. As we further increased the undercooling, a morphological change from dendritic to equiaxed grains of the primary α -Al phase with fibrous eutectic Si was observed.²⁴ This morphological change was also observed to occur in other rapid solidification studies of Al-Si alloys.^{25,26} As a result of the large

thermal gradients and undercooling induced by the SLM process, the preferred solidification structure is the α -dendritic structure, observed in Fig. 5. Studies on the solidification of Al-Si (A356 and Al-11.3Si-2Cu-0.4Fe) systems have determined cooling curves from T_m to $0.9T_m$ for the solidification phenomenon at a cooling rate of approximately 5°C/s .^{13,27} The authors determined that when the solidification of the primary α -phase began, the evolution of the latent heat from the formation of the primary phase retarded the cooling rate and increased the temperature of the melt. Once the initial latent heat was removed a constant cooling rate was achieved.^{13,27} In the case of the P-SLM Al-12Si, the molten pool boundary observed is believed to be a result of the initial removal of latent heat from the molten pool, a clear demonstration of the recalescence phenomena. Solidification begins as the latent heat begins to be removed from the molten pool, during which the solidification rate would be slower, until completed, at which point the solidification rate would increase to complete the process as the temperature drops, leaving a coarsened area along the edge of each pulse boundary.

Thermal gradients and undercooling values generated by the incident pulse result in a modification of the preferred primary solidification phase from

eutectic to α -dendritic and takes the form of the predominantly dendritic microstructure presented in Fig. 5. The thermal gradient (G) experienced and the rate at which the solid–liquid interface advances (R) greatly affect the resultant morphology and scale of the microstructure.²⁸ Kurz, Gionvanola, and Trivedi (KGT) developed a model to describe the microstructural development during solidification based on the R and G .²⁹ Because of the nature of the process, the exact temperature that the molten pool experiences is difficult to measure. One can assume, however, that the temperature achieved will be lower than that of the vaporization temperature of Al (2300°C). Assuming a temperature of 2000°C at the highest point, similar to that of Matsunawa et al.,³⁰ and for an average pulse penetration depth of 200 μm measured from optical imaging, a thermal gradient of approximately 10^6 K/m would arise. The KGT curve for the Al-Si system with this G is shown in Fig. 6. Based on the scale of the microstructure, one can then infer the relative velocity of the solidification front (solid/liquid interface) experienced during solidification of center of the pulses. The dendrite tip radius measured from Fig. 5 falls directly in the fine dendritic region predicted by the KGT model, confirming the observations of the microstructure. From the spacing measured from Fig. 5, an average solidification rate of 1×10^{-3} m/s can be inferred in the center of the pulse and 1×10^{-4} m/s along the boundary of the molten pool. The cooling rate experienced can then be estimated as the product of $G \times R$. Therefore, an estimate of the initial cooling rate as solidification begins is 1×10^2 K/s at the boundary of the pulse, which then increases 1×10^3 K/s after recalescence completes. Based on the solidification velocity measured, we can then determine the life of the molten

pool, which for an average depth of 200 μm should last for approximately 10 ms.

Table II presents a comparison of the microstructural scale obtained using P-SLM compared to CW-SLM. The comparison demonstrates that the pulsed laser results in more refined Si microstructural features than the CW laser. Based on the KGT model, the solidification front velocity measured from the CW microstructures was found to be on the order of 5×10^{-5} m/s compared with the P-SLM of 1×10^{-3} m/s. Because of the faster cooling rates of the pulsed laser, the Si arm thickness (70 ± 20 nm) and Al cell spacing (210 ± 60 nm) showed twice the refinement compared with the reported values of CW SLM studies (Si arm thickness 200 nm and Si cell spacing 500–1000 nm).^{31,32}

Hardness comparisons are shown in Table III, depicting that near full-density P-SLM Al-12Si parts can be achieved with superior hardness values compared with a typical cast Al-12Si part (64 ± 4 HV).²² The P-SLM components achieved hardness values of 135 ± 5 HV for the samples with the highest density. The microhardness values were higher than previously reported values of Al-12Si SLM parts using CW lasers at ~ 55 – 107 HV⁹ and ~ 115 HV.¹⁶ A similar concept has been demonstrated by Karaköse et al.,³³ where further increases in microhardness were obtained by refining Si grain size though rapid solidification process in Al-8Si-1Sb alloy. As the hardness of Al-Si alloys greatly depend on not only the grain size but also the size and distribution of the Si phase throughout the matrix.¹¹ The refined scale of both the Al and Si phases resulted in comparable hardness values at a lower density than those reported by Prashanth et al.³² These results show evidence that the P-SLM could promote improved mechanical properties due to

Table II. Comparison of the geometrical features between P-SLM and CW-SLM Al-12Si alloys

	P-SLM (This work)	CW-SLM ^{31,32}
Composition	Al-12Si	Al-12Si
Morphology	Dendritic structure	Dendritic structure
Si arm thickness	70 ± 20 nm	200 nm
Al spacing	210 ± 60 nm	500–1000 nm

Table III. The density of the P-SLM components compared to CW SLM Al-Si alloys

Alloy	Condition	Density (%)	Hardness (HV)	Reference(s)
Al-12Si (S20)	P-SLM	93.8 ± 1.9	135 ± 5	This work
Al-12Si (S10)	P-SLM	95.6 ± 1.0	135 ± 5	This work
Al-12Si	SLM—CW	60–80	55–107	9
Al-12Si	SLM—CW	97	115	16
Al-12Si	SLM—CW	99.5	130	31,32

the more rapid cooling rates achieved compared with a CW laser.

SUMMARY

P-SLM was used successfully to additively manufacture a binary Al-12Si alloy and was compared with that of CW-SLM. Two different particle size distributions were tested, with the larger particle size requiring a larger laser power for sufficient densification. The density of the final part depended on the energy density applied to a maximum after which a slight drop in density was observed. The final part showed an increase in hardness compared with the traditional cast alloy and other SLM studies. The solidification phase and morphology of the final microstructure was modified based on the large undercooling, thermal gradients, and solidification front velocities expected to develop.

ACKNOWLEDGEMENT

The authors would like to thank AUTO21 (Grant C502-CPM) for financial support of this research.

REFERENCES

1. J.P. Kruth, M.C. Leu, and T. Nakagawa, *CIRP Ann. Manufact. Tech.* 47, 525 (1998).
2. D.D. Gu, W. Meiners, K. Wissenbach, and R. Poprawe, *Int. Mater. Rev.* 57, 133 (2012).
3. K.V. Wong and A. Hernandez, *ISRN Mech. Eng.* 2012, 10 (2012).
4. I. Gibson, D.W. Rosen, and B. Sucker, *Additive Manufacturing Technologies: Rapid Prototyping to Direct Digital Manufacturing* (New York: Springer, 2010).
5. E. Louvis, P. Fox, and C.J. Sutcliffe, *J. Mater. Process. Tech.* 211, 275 (2011).
6. E. Brandl, U. Heckenberger, V. Holzinger, and D. Buchbinder, *Mater. Des.* 34, 159 (2012).
7. D. Buchbinder, H. Schleifenbaum, S. Heidrich, W. Meiners, and J. Bültmann, *Phys. Procedia* 12, 271 (2011).
8. K. Kempen, L. Thijs, J. Van Humbeeck, and J.P. Kruth, *Phys. Procedia* 39, 439 (2012).
9. E.O. Olakanmi, R.F. Cochrane, and K.W. Dalgarno, *J. Mater. Process. Tech.* 211, 113 (2011).
10. L. Thijs, K. Kempen, J.-P. Kruth, and J. Van Humbeeck, *Acta Mater.* 61, 1809 (2013).
11. M. Warmuzek, *Aluminum-Silicon Casting Alloys: Atlas of Microfractographs* (Materials Park, OH: ASM International, 2004).
12. M. Salehi, K. Dehghani, and J. Alloy, *Compd.* 457, 357 (2008).
13. J. Xu, F. Liu, D. Zhang, and Z. Jian, *J. Therm. Anal. Calorim.* (2014).
14. H.J. Niu and I.T.H. Chang, *J. Mater. Sci.* 35, 31 (2000).
15. A. Manthiram, D.L. Bourell, and H.L. Marcus, *JOM* 45 (11), 66 (1993).
16. X.J. Wang, L.C. Zhang, M.H. Fang, and T.B. Sercombe, *Mater. Sci. Eng. A* 597, 370 (2014).
17. A. Simchi, *Mater. Sci. Eng. A* 428, 148 (2006).
18. X. Liu, P.K. Chu, and C. Ding, *Mater. Sci. Eng. R* 47, 49 (2004).
19. J.-P. Kruth, M. Badrossamay, E. Yasa, J. Deckers, L. Thijs, and J. Van Humbeeck, *Proceedings of the 16th International Symposium on Electromachining* (Shanghai, China: Shanghai Jiao Tong University Press, 2010).
20. D. Manfredi, F. Calignano, M. Krishnan, R. Canali, E. Ambrosio, and E. Atzeni, *Materials* 6, 856 (2013).
21. W. Shifeng, L. Shuai, W. Qingsong, C. Yan, Z. Sheng, and S. Yusheng, *J. Mater. Process. Tech.* 214, 2660 (2014).
22. J. Milligan, J.M. Shockley, R.R. Chromik, and M. Brochu, *Tribol. Int.* 66, 1 (2013).
23. F.A. España, V.K. Balla, and A. Bandyopadhyay, *Philos. Mag.* 91, 574 (2010).
24. H.S. Kang, W.Y. Yoon, K.H. Kim, M.H. Kim, and Y.P. Yoon, *Mater. Sci. Eng. A* 404, 117 (2005).
25. Y. Birol, *J. Mater. Sci.* 31, 2139 (1996).
26. F. Yilmaz and R. Elliott, *J. Mater. Sci.* 24, 2065 (1989).
27. S. Nafisi and R. Ghomashchi, *Mater. Character.* 57, 371 (2006).
28. S. Kou, *Welding Metallurgy*, 2nd ed. (New York: Wiley, 2003).
29. W. Kurz, B. Giovanola, and R. Trivedi, *Acta Metall.* 34, 823 (1986).
30. A. Matsunawa, M. Mizutani, and S. Katayama, *Trans. JWRI* 25, 161 (1996).
31. K.G. Prashanth, S. Scudino, H.J. Klauss, K.B. Surreddi, L. Löber, Z. Wang, A.K. Chaubey, U. Kühn, and J. Eckert, *Mater. Sci. Eng. A* 590, 153 (2014).
32. K.G. Prashanth, B. Debalina, Z. Wang, P.F. Gostin, A. Gebert, M. Calin, U. Kühn, M. Kamaraj, S. Scudino, and J. Eckert, *J. Mater. Res.* 29, 2044 (2014).
33. E. Karaköse and M. Keskin, *J. Alloy Compd.* 479, 230 (2009).